Integrated bioinformatic analysis for the identification of potential biomarkers of kidney damage in hyperoxaluria

Usha Adiga[1], Shreyas Adiga[2*], Thayyil Menambath Desy[3], Neha Honnalli[3], Tirthal Rai[1]

[1]Department of Biochemistry, KS Hegde Medical Academy, Nitte-DU, Mangalore, India.
[2]International Institute of Information Technology, Hyderabad, India.
[3]Department of Biochemistry, KS Hegde Medical Academy, ICMR, Nitte-DU, Mangalore, India.

ARTICLE HISTORY

ABSTRACT

Hyperoxaluria is described by an augmented urinary elimination of oxalate. Systemic oxalosis is the term for the condition that occurs when the burden of calcium oxalate (CaOx) surpasses the renal capacity to excrete it. When individuals acquire chronic renal disease, elevated urinary oxalate levels aid in diagnosis, whereas plasma oxalate levels are probably more reliable. Based on bioinformatic analysis, the study aimed to identify differentially expressed genes (DEGs) and miRNA as potential biomarkers to differentiate normal versus hyperoxaluric state compared to the stage of CaOx crystals in the kidney. Published microarray data for gene expression patterns of normal controls, hyperoxaluric kidney tissue, and kidney tissue at the stage of crystal formation were collected from the National Center for Biotechnology Information Gene Expression Omnibus database. Integrated bioinformatics methods were utilized to analyze and compare these gene expression patterns. The data processing was conducted using R software. Gene ontology and the Kyoto Encyclopedia of Genes and Genomes database were employed to explore the enrichment of pathways and functions in the DEGs. Additionally, the STRING database was utilized to investigate protein–protein interactions. Tarbase, Mirnda, and DIANA software were used to obtain miRNAs for the top 10 DEGs. A total of 62,966 genes were screened, 2,814 were differentially expressed, out of which 603 genes were statistically significantly differentially expressed, after analyzing the GSE89028 dataset. A total of 2,810 genes were downregulated and only 4 genes were upregulated on day 14. The genes Cdt1 and cdhr4 were highly significantly differentiated with log2 (fold change) being −3.085 and −3.966, respectively, −log 10 (p-value) being 6.857 and 6.196, respectively, at 14 days. On day 28, 62,976 genes were screened, out of which 356 were significantly differentiated. Only four genes were upregulated and 240 genes were downregulated. Csmd1, Olr154, Cntfr, Zbtb16 log2 (fold change) being 1.188, 1.527, 1.782, and 2.636, respectively; −log 10 (p-value) being 4.071, 3.804, 4.357, and 4.061, respectively. The text mining evidence was observed on string analysis in both the contexts. The strength of alternative splicing (cellular enrichment) was 1.16 with a false discovery rate of 0.0409. The study showcases the effectiveness of bioinformatics analytical methods in pinpointing potential pathogenic genes associated with hyperoxaluria and the deposition of crystals in the kidneys. The interaction network identified two miRNAs, hsa-miR-6884-5p and hsa-miR-4653-5p, and two genes CDHR4 and EGR2 as significant players.

INTRODUCTION

Oxalate, which comes from a variety of plant and animal sources and is primarily removed via the kidneys, is the ionic form of oxalic acid. A metabolic disease called hyperoxaluria is characterized by an elevated excretion of oxalate through the urine. Healthy people typically excrete between 10 and 40 mg of oxalate every 24 hours. Clinical hyperoxaluria is defined as concentrations that are greater than 40–45 mg per 24 hours [1–3]. This may be the result of greater intestinal absorption or improved ingestion of precursors of oxalate in hyperoxaluria due to secondary causes or increased endogenous oxalate synthesis in primary hyperoxaluria.

*Corresponding Author
Shreyas Adiga, IIIT, Hyderabad, India.
E-mail: shreyas.adiga @ research.iiit.ac.in*

If not treated properly, end-stage renal disease (ESRD), which can manifest in the sixth decade of life or as early as infancy, can result from hyperoxaluria, which has the potential to have devastating consequences [4]. Nephrocalcinosis, urinary tract infections, recurrent kidney stones, as well as chronic kidney disease (CKD) and end-stage renal disease, are among the variety of illnesses. Oxalate deposits in a number of organ systems are caused by elevated plasma oxalate levels. Although systemic oxalosis should be prevented, more than 40% of patients experience a diagnostic delay. As per the survey by Hoppe *et al.* [5], 30% of the subjects were only diagnosed after they had already developed ESRD. When the disease reappears after a kidney transplant, the diagnosis may occasionally be made for the first time [6]. A great index of doubt and a prompt diagnosis are necessary for the proper treatment of hyperoxaluria, which is still a difficult condition to manage.

Increased urinary oxalate excretion characterizes the disease known as hyperoxaluria. When oxalate intake is increased, its precursors are consumed more frequently, or the gut flora is altered, and secondary hyperoxaluria develops. An inherited defect in the metabolism of oxalate is primary hyperoxaluria. These illnesses can cause nephrocalcinosis, recurring kidney stones, and ultimately end-stage renal disease. Despite these similarities, each subtype of hyperoxaluria has a unique pathophysiology, clinical presentation severity, and therapeutic strategy.

Early clinical diagnosis and differentiation of these illnesses are crucial for timely intervention and have an impact on the prognosis of individuals with hyperoxaluria.

Renal damage and inflammation brought on by hyperoxaluria brought on by calcium oxalate (CaOx) crystal deposition in the kidneys results in a range of illnesses, including CKD. However, it has been unable to distinguish between the renal effects of CaOx crystal deposition and hyperoxaluria. Joshi *et al.* [7] used the ethylene glycol (EG) model, which allows the timing of both hyperoxaluria and the formation of CaOx crystals.

To test this theory, male rats were given EG to induce hyperoxaluria. Rats were then killed, and kidneys were removed on days 14 and 28 when all of the animals had acquired renal CaOx crystal deposits. Total ribonucleic acid (RNA) was gathered to conduct microarray and genome-wide analysis, aiming to identify differentially expressed genes (DEGs) and compare the variations between hyperoxaluria and kidney changes induced by crystals.

Aim

To use microarray data (deposited by the author Joshi *et al.* [7]) for bio-informatic analysis to find DEGs that are associated with renal impairment in the hyperoxaluric stage as compared to oxalate crystal formation stage as compared to that in normal controls. The study also aimed to study gene enrichment, gene ontology (GO), KEGG pathway improvement, protein collaboration protein–protein interaction (PPI) organizations, and miRNA-target quality cooperation organizations to learn more about the underlying molecular mechanisms of hyperoxaluria as compared to oxalate crystal formation stage.

METHODOLOGY

Microarray data

Chips, high-throughput microarrays, and data on gene expression can all be found in the public and functional genomics database known as the Gene Expression Omnibus. The GSE89028 microarray data were downloaded https://www.ncbi.nlm.nih.gov/geo/ for evaluation in this study. This dataset was deposited by Joshi *et al.* [7]. There were three groups of male rats in the study (imp), one being the control group, the other one administered with EG, and the third group on EG and spironolactone (ES). All the groups were investigated on days 14 and 28 for gene expression patterns by microarray analysis.

Data processing

To process raw data and screening DEGs, the statistical software R4.0.1 (https://www.r-project.org/) and a Bioconductor (http://bioconductor.org/biocLite.R) were utilized. The Limma package was used to calibrate and standardize the data in batches. The fundamental aspect of the Limma package is to apply a linear model to gene expression data to assess its potential for differential expression [8]. Reading, standardizing, and analyzing such data is made easy with the Limma package's powerful tools. A Limma package was then used to filter the genes with different levels of expression. The fold-change and *p*-value of less than 0.05 were the screening criteria. The DEGs were displayed on a volcano map using the ggplot2 package, and the significant DEGs were clustered using the heatmap package.

Evaluation of enrichment of pathways and function of DEGs

The Gene Ontology [http://www.geneontology.org], a resource for bioinformatics that is based on the community was used. It uses ontology to expand our understanding of biology and provides information about the functions of genes and gene products [9]. An information base for the subjective translation of genomic successions and other natural information, the Kyoto Encyclopedia of Genes and Genomes (KEGG) (https://www.kegg.jp/) includes information about systematic, genomic, chemical, and a supplementary human-specific categories of health information [10]. The GO/KEGG enrichment and cluster Profiler software package were employed to examine the relevant signaling pathways and biological functions. A *p*-value equal to or greater than 0.05 is deemed statistically significant in the analysis.

Building a network of PPIs and identifying and confirming hub genes

PPI network analysis significantly enhances the prediction of protein functions and their interactions. This valuable tool helps researchers gain insights into cellular and disease mechanisms [11,12]. The STRING database (http://string-db.org) plays a vital role in this context by integrating a vast amount of known and predicted protein–protein association data, offering a comprehensive evaluation of protein interactions [13,14]. The obtained PPI network, constructed using the STRING database, can be visualized in Cytoscape. Additionally, the cytohubba module of the Cytoscape programming was utilized to separate center qualities with a higher score in this investigation, indicating that these genes are more connected to PPI networks.

The statistical significance of these genes was confirmed using GEO2R, an interactive network tool that enables users to compare two or more sets of samples in a GEO sequence to identify DEGs [15]. It was deemed statistically significant if $p < 0.05$.

MicroRNA (miRNA)-target gene network

A type of small endogenous non-coding RNA known as miRNA has between 18 and 25 nucleotides. At the post-transcriptional levels, it is the primary central regulator. It is involved in numerous biological processes, including apoptosis, cell differentiation, and the cell cycle [16,17]. The miRDB, DIANA, and TargetScan database contain detailed metadata, experimental methods, and conditions, as well as manually managed and experimentally validated interactions between genes and miRNAs [18]. These databases were used to construct the miRNA–gene targeting relationship for overlapping differential genes and hub genes.

RESULTS AND DISCUSSION

A total of 62,966 genes were screened, 2,814 were differentially expressed, out of which 603 genes were statistically significantly differentially expressed, after analyzing the GSE89028 dataset (Fig. 1a). A total of 2,810 genes were downregulated and only 4 genes were upregulated on day 14.

A volcano plot visually presents the relationship between statistical significance (expressed as −log10 p-value) and the magnitude of change (log2 fold change) in gene expression. It serves as a valuable tool for visualizing and identifying DEGs. GSE89028 was used to screen DEGs (upregulated and Generated using Limma).The genes Cdt1 and cdhr4 were highly significantly differentiated with log2 (fold change) being −3.085 and −3.966 respectively, −log 10 (p-value) being 6.857 and 6.196, respectively, at 14 days.

On day 28, 62,976 genes were screened, out of which 356 were significantly differentiated (Fig. 1b). EGR2 and DIO3 were highly expressed with a false discovery rate (FDR) of 0.0156 and 817 fold enrichment. Only four genes were upregulated and 240 genes were downregulated. Csmd1, Olr154, Cntfr, and Zbtb16 log2 (fold change) being 1.188, 1.527, 1.782, and 2.636, respectively; −log 10 (p-value) being 4.071, 3.804, 4.357, and 4.061, respectively. At a cutoff (by default) of
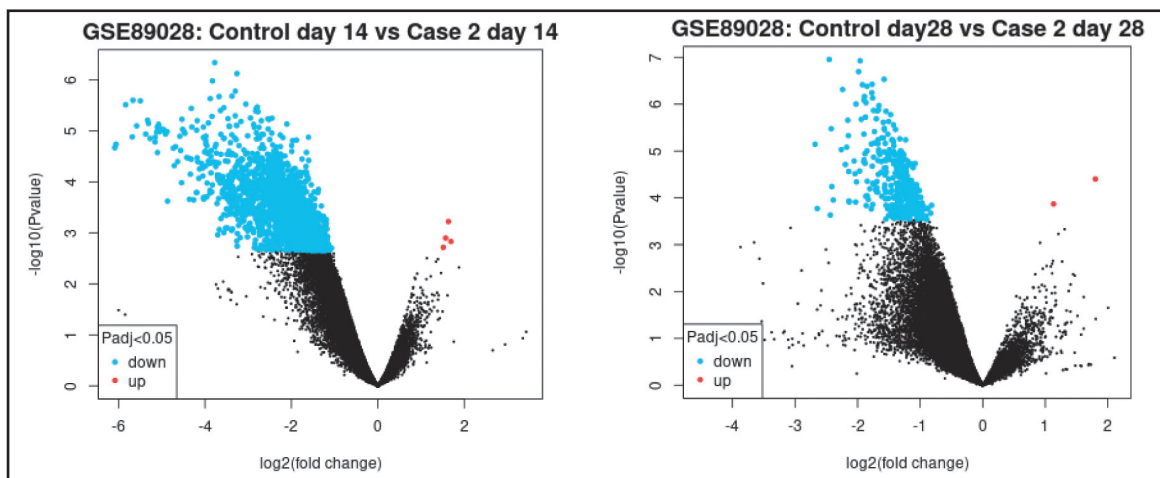

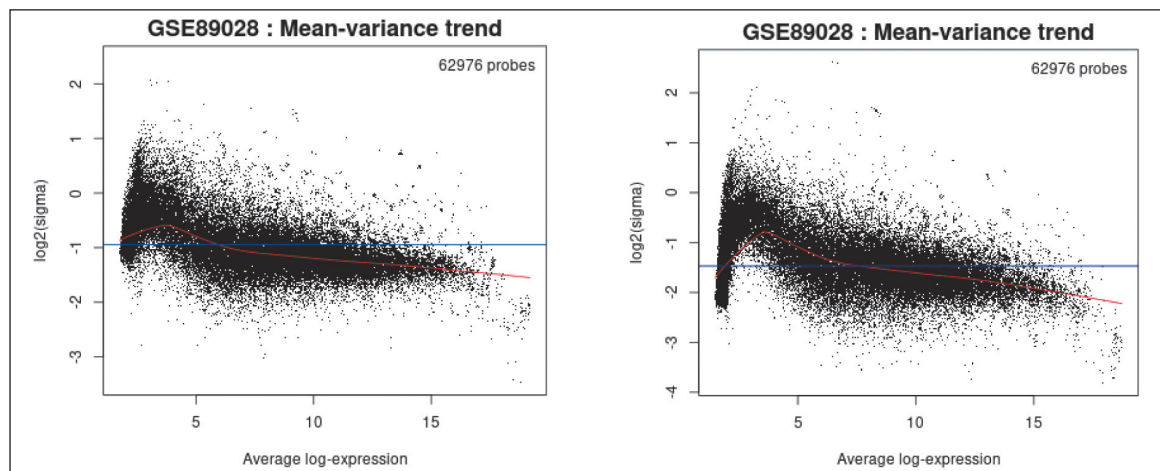**Figure 1.** (a) Volcano plot on the 14th day. (b) Volcano plot on the 28th day.

Figure 2. (a) MD on the 14th day. (b) MD on the 28th day.

an adjusted *p*-value was 0.05, genes that are highlighted exhibit significant differential expression (red indicates upregulation and blue indicates downregulation).

Data points beyond 1 imply ratio of means is higher than 2 fold or more. Points on the negative log imply half fold increase. *p*-values become smaller and smaller with increasing significance. The top upper two quadrants are significant.

The log2 fold change in contrast to the average log2 expression value is shown in a mean difference (MD) plot (Fig 2a and b) created with Limma (plotMD), which helps demonstrate DEGs.

A mean distinction plot shows the test results for a solitary difference and compares the disagreement or differences between two quantitative measurements, i.e., the expression of genes. Blue lines suggest MD, being −0.9 and −1.5, respectively, on days 14 and 28. Red lines indicate ±1.96 standard deviations from MD.

Limitation

Plotting data for up to five contrasts is possible. When more than five groups have been identified, the default action is to display contrasts between the genes with the highest and lowest expression numbers.

R boxplot was used to generate the boxplot (Fig. 3a and b). It was used to see the distribution of the values of the selected samples. The samples are arranged in groups by color. To know if the Samples chosen are suitable for differential expression analysis, taking a look at the distribution can be helpful. In most cases, values that are centered on the median indicate that the data can be cross-comparable and normalized.

The plot shows data after log transform and normalization, if they were performed.

Expression density plot (Fig. 4a and b), made with R Limma (plotDensities), to see how the values of the selected samples are distributed. The samples are arranged in groups by
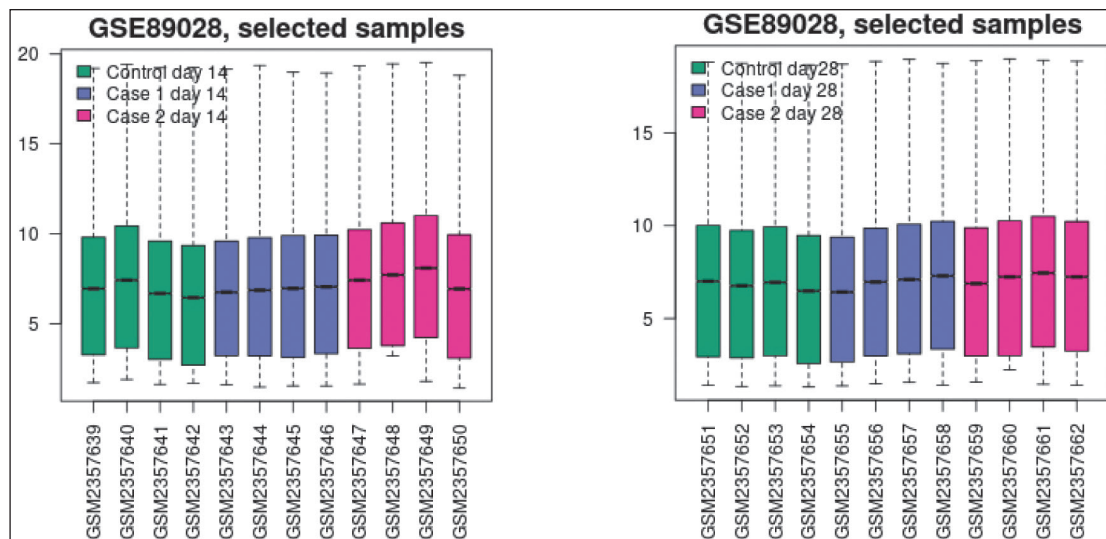

Figure 3. (a) Box plot on the 14th day. (b) Box plot on the 28th day.
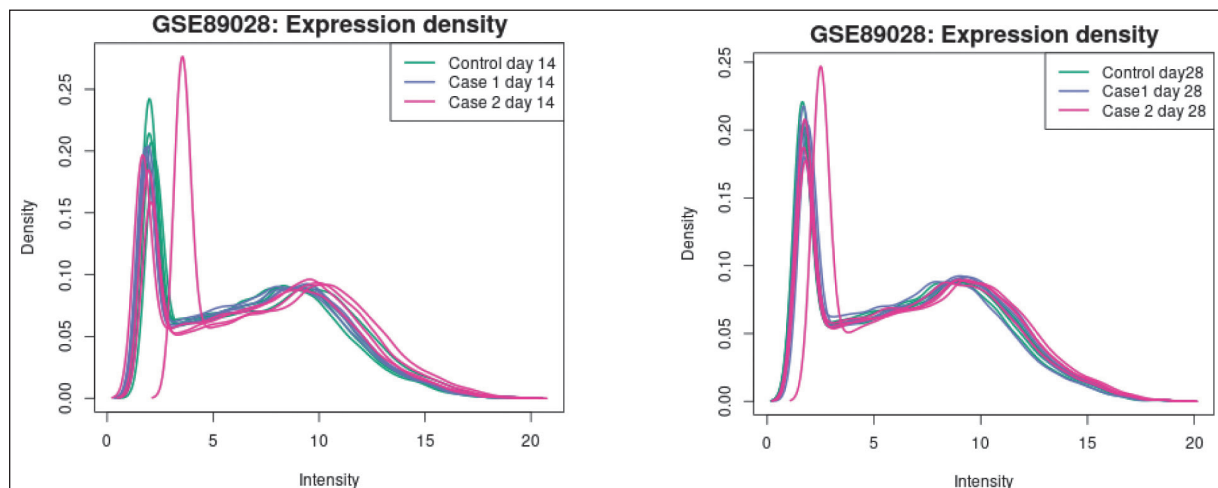

Figure 4. (a) Expression density plots on the 14th day. (b) Expression density plots on the 28th day

color. In checking for data normalization prior to differential expression analysis, this plot works in tandem with the boxplot above.

Histogram (Fig. 5)—Created with hist—used to see how the distribution of *p*-values in the analysis results. All selected contrasts were used to calculate the *p*-value, which is identical to that in the top DEGs table.

Moderated *t*-statistic quantile–quantile plot; q–q plot (Fig. 6)—produced with the help of Limma, qqt plots a data sample's quantiles against the theoretical quantiles of a Student's *t* distribution. The quality of the Limma test results can be evaluated using this plot.

Following the application of a linear model, an R Limma function (plotSA, vooma) is utilized to generate a mean-variance plot, which serve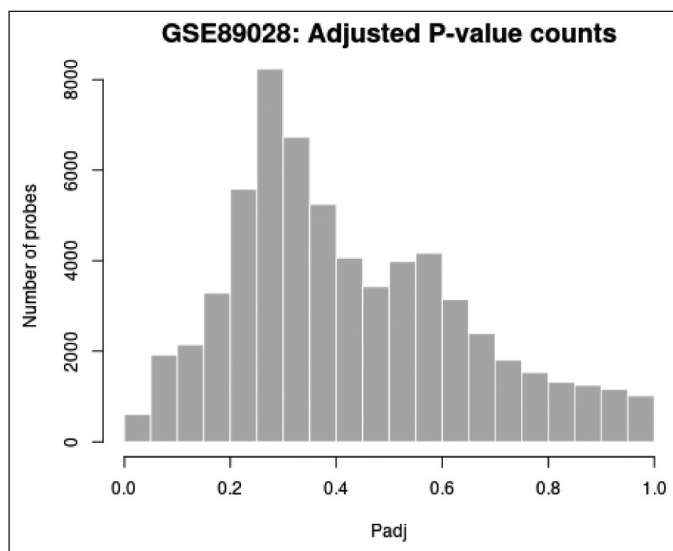s to validate the correlation betwe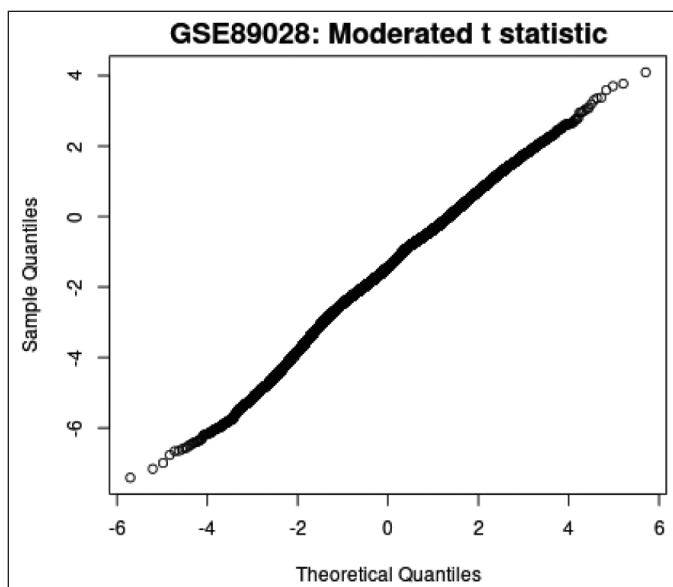en the mean and variance of the expression data. It may be helpful to demonstrate that there is a lot of variation in the data. This graph helps in evaluating whether it is advisable to utilize the precision weights option to address the mean-variance trend. When a significant mean-variance trend exists, employing precision weights enhances the reliability of the test outcomes.

Each point in the plot represents a gene. The red line depicts the mean-variance trend approximation, which considers or has already considered the precision weight option from the Options tab during the analysis of differential gene expression. On the other hand, the blue line represents an approximation of constant variance.

Generated with the help of Uniform Manifold Approximation and Projection (UMAP), UMAP (Fig. 7a and b) is a useful method for reducing the number of dimensions and making it easier to see how Samples are related to one another. It reduces the data to two dimensions. The plot shows how many closest neighbors were used in the calculation.

By utilizing the Limma algorithm (Venn diagram) (Fig 8a and b) to browse and download the substantial gene overlap between various contrasts Venn diagram is plotted. Out of 2,812 genes, 2 genes were common between cases on EG and cases both on EG and spironolactone. There were no common genes expressed between other groups.

In contrast to day 14, 129 genes were common for controls of cases on EG and cases on both EG and spironolactone, 2 genes each for controls compared to cases on EG and cases on both EG and spironolactone on day 28.

The top 10 genes expressed at days 14 and 28 along with their associated miRNA s are represented in Tables 1 and 2, respectively.

Based on GO enrichment analysis, the gene association displayed a strength of 0.91, and the FDR was 0.0373. The genes showed enrichment in various pathways, including the mitogen-activated protein kinase signaling pathway, the PI3K-Akt pathway, the RAP 1 signaling pathway, the cyclic adenosine monophosphate signaling pathway, and multiple metabolic pathways. Additionally, biological processes such as the intrinsic apoptotic signaling pathway responding to DNA damage, signal transduction by p53, with FDR values ranging from 0.018 to 0.0259 and a strength of 1.58 to 2.0. Cellular component enrichment revealed the transcription regulator complex with a strength of 0.91 and an FDR of 0.0373.

On day 14, a total number of nodes were 9, a number of edges 2 (versus projected number zero), the average local clustering coefficient was 0.22, the average node degree was 0.44, and the PPI enrichment *p*-value was 0.0738 in the string database analysis (Fig. 9). The strength of cellular enrichment (condensed chromosome kinetochore) was 1.85 with a false discovery rate of 0.0160.

In contrast, on day 28, observed nodes were 7, edges 1 (versus 0), the average node degree, as well as average local clustering coefficient, was 0.286, PPI enrichment *p*-value being 0.11 (Fig. 10).

The network's nodes are proteins. The edges represent the hypothesized functional relationships. Seven colored lines were used to draw an edge in evidence mode; The following lines denote the presence of the seven distinct types of evidence
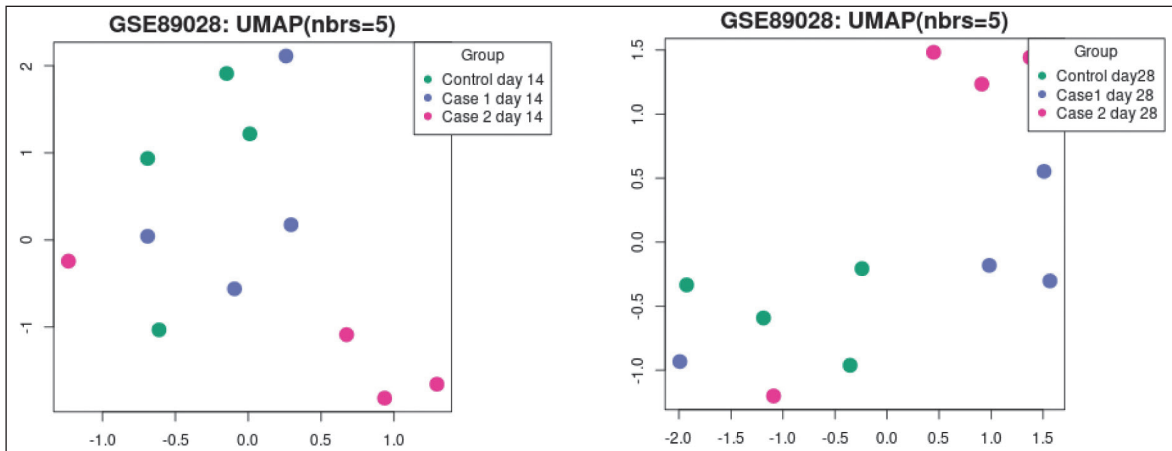

Figure 5. Histogram for *p*-value distribution.

Figure 6. q–q plot.

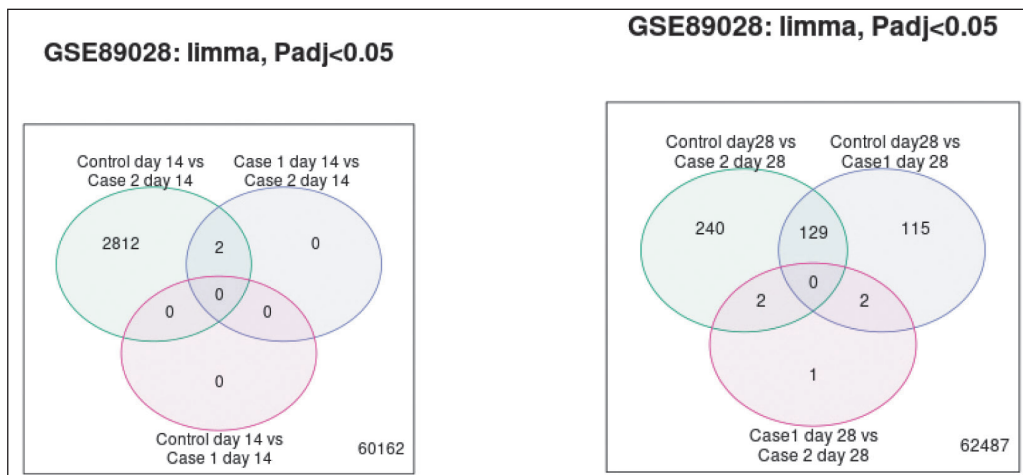**Figure 7.** (a) UMAP plot at day 14. (b) UMAP plot at day 28.

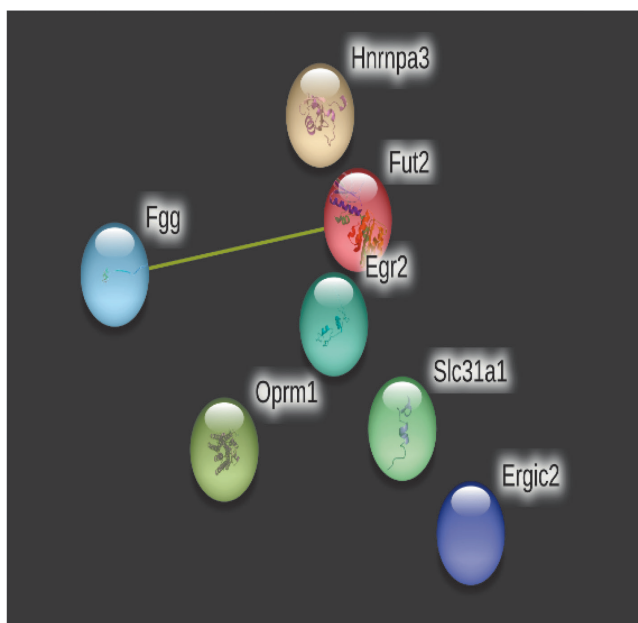**Figure 8.** (a) Venn diagram comparing DEGs on day 14. (b) Venn diagram comparing DEGs at day 28.

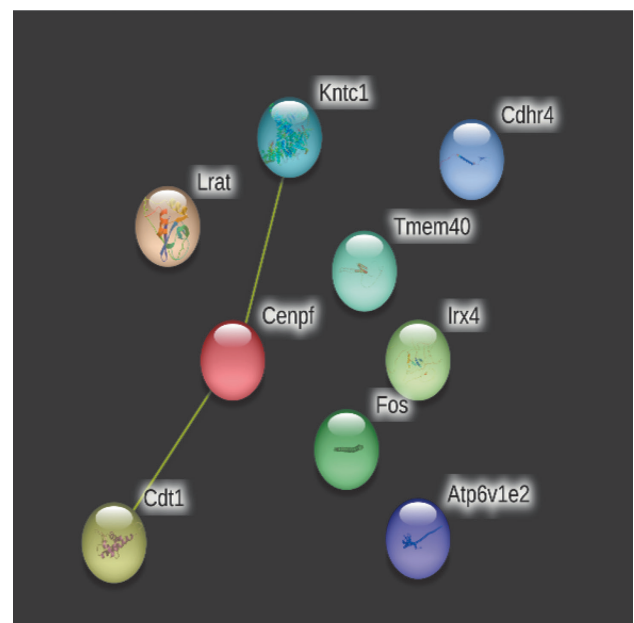**Figure 9.** PPIs of top 10 genes on day 14.

Figure 10. PPIs of top 10 on day 28

Table1. Enrichment of top 10 genes and their associated miRNAs on day 14.

Enrichment FDR	Fold Enrichment	Pathway	Genes	
0.0185	417.64	Mixed, incl. pea3 subfamily ets-domain transcription factor n terminal domain, a	Cdhr4	hsa-miR-3133,hsa-miR-3613-3p,hsa-miR-6866-5p,hsa-miR-4472, hsa-miR-4447, hsa-miR-6884-5p, hsa-miR-3150a-3p, hsa-miR-340-3p,hsa-miR-4326, hsa-miR-2467-5p,
0.0185	417.64	Magnesium chelatase, subunit ChlI	Cdt1	hsa-miR-6076,hsa-miR-6775-3p,hsa-miR-1291
				hsa-miR-4731-5p,hsa-miR-4493,hsa-miR-6778-3p,hsa-miR-6879-3p
0.0185	417.64	Jun-like transcription factor, and bZIP Maf transcription factor	Fos	hsa-miR-589-3p, hsa-miR-4802-3p,hsa-miR-335-3p, hsa-miR-155-5p, hsa-miR-101-3p
				hsa-miR-5006-5p, hsa-miR-5590-3p, hsa-miR-3200-5p, hsa-miR-569
				hsa-miR-1298-5p
0.0185	417.64	Lecithin retinol acyltransferase	Lrat	hsa-miR-4282,hsa-miR-3121-3p, hsa-miR-153-5p, hsa-miR-23b-3p, hsa-miR-23a-3p, hsa-miR-3148, hsa-miR-23c
				hsa-miR-1284, hsa-miR-3606-3p, hsa-miR-3163
0.0189	348.03	Motif in Iroquois-class homeodomain proteins (only). Unknown function.	Irx4	hsa-miR-423-5p, hsa-miR-519d-3p, hsa-miR-526b-5p, hsa-miR-6780a-3p, hsa-miR-8072, hsa-miR-93-5p
				hsa-miR-526b-3p, hsa-miR-4276, hsa-miR-20a-5p, hsa-miR-6739-3p
0.0189	298.31	Mixed, incl. retinal pigment epithelial membrane protein, and lecithin retinol a	Lrat	hsa-miR-4282, hsa-miR-3121-3p, hsa-miR-153-5p, hsa-miR-23b-3p, hsa-miR-23a-3p
				hsa-miR-3148, hsa-miR-23c, hsa-miR-1284
				hsa-miR-3606-3p,
				hsa-miR-3163
0.0189	298.31	Mixed, incl. transmembrane protein 40 family, and domain of unknown function (du	Tmem40	hsa-miR-325-3p, hsa-miR-138-5p, hsa-miR-6893-3p, hsa-miR-370-3p
0.0198	261.03	Ion transport protein N-terminal, and T-box transcription factor	Irx4	hsa-miR-30e-5p, hsa-miR-30d-5p, hsa-miR-30a-5p, hsa-miR-30b-5p, hsa-miR-30c-5p, hsa-miR-520d-3p, hsa-miR-302e, hsa-miR-372-3p, hsa-miR-520a-3p, hsa-miR-4276, hsa-miR-512-3p
0.0222	208.82	Mixed, incl. aurora-a binding, and k167/ chmadrin repeat	Cenpf	hsa-miR-205-5p, hsa-miR-520f-3p
0.0222	174.02	Retinal pigment epithelial membrane protein, and Retinol metabolism	Lrat	hsa-miR-4282, hsa-miR-3121-3p, hsa-miR-153-5p, hsa-miR-23b-3p, hsa-miR-23a-3p, hsa-miR-3148, hsa-miR-23c, hsa-miR-1284
				hsa-miR-3606-3p, hsa-miR-3163
0.0280	122.84	Mixed, incl. microtubule binding, and aurora-a binding	Cenpf	hsa-miR-205-5p
				hsa-miR-520f-3p
0.0280	116.01	Retinol metabolism, and CRAL/TRIO, N-terminal domain	Lrat	hsa-miR-4282, hsa-miR-3121-3p, hsa-miR-153-5p, hsa-miR-23b-3p, hsa-miR-23a-3p, hsa-miR-3148, hsa-miR-23c, hsa-miR-1284
				hsa-miR-3606-3p, hsa-miR-3163
0.0280	116.01	MCM OB domain, and GINS complex protein	Cdt1	hsa-miR-6076, hsa-miR-6775-3p, hsa-miR-1291, hsa-miR-4731-5p
				hsa-miR-4493, hsa-miR-6778-3p, hsa-miR-6879-3p
0.0281	109.91	Collecting duct acid secretion, and V-ATPase subunit H	Atp6v1e2	hsa-miR-203a-5p, hsa-miR-6501-3p, hsa-miR-548at-5p, hsa-miR-27a-5p
0.0295	87.01	Collecting duct acid secretion	Atp6v1e2	hsa-miR-203a-5p, hsa-miR-6501-3p, hsa-miR-548at-5p, hsa-miR-27a-5p
0.0295	77.34	Connexin, and Ion transport protein N-terminal	Irx4	hsa-miR-30e-5p, hsa-miR-30d-5p, hsa-miR-30a-5p, hsa-miR-30b-5p, hsa-miR-30c-5p
				hsa-miR-520d-3p, hsa-miR-302e, hsa-miR-372-3p, hsa-miR-520a-3p, hsa-miR-4276, hsa-miR-512-3p
0.0295	63.28	Mostly uncharacterized, incl. nnf1 , and yippee zinc-binding/dna-binding /mis18,	Kntc1	hsa-miR-6884-5p, hsa-miR-485-5p, hsa-miR-138-5p, hsa-miR-370-3p, hsa-miR-6893-3p, hsa-miR-421, hsa-miR-505-3p.2, hsa-miR-494-3p, hsa-miR-19b-3p, hsa-miR-19a-3p, hsa-miR-205-5p

Continued

Enrichment FDR	Fold Enrichment	Pathway	Genes	
0.0143	61.42	Mixed, incl. microtubule binding, and cyclin, c-terminal domain	Cenpf Fam64a	hsa-miR-205-5p, hsa-miR-520f-3p, hsa-miR-330-3p, hsa-miR-668-3p, hsa-miR-371a-5p
				hsa-miR-493-5p
0.0019	46.75	Mixed, incl. cell cycle, and microtubule binding	Cenpf Kntc1 Fam64a	hsa-miR-6884-5p, hsa-miR-485-5p, hsa-miR-138-5p, hsa-miR-370-3p, hsa-miR-6893-3p,
				hsa-miR-421, hsa-miR-505-3p.2, hsa-miR-494-3p, hsa-miR-19b-3p, hsa-miR-19a-3p,
				hsa-miR-205-5p, hsa-miR-205-5p, hsa-miR-520f-3p, hsa-miR-330-3p, hsa-miR-668-3p, hsa-miR-371a-5p, hsa-miR-493-5p

that were taken into account when anticipating the relationships. The red line indicates the presence of fusion evidence, neighborhood evidence in green, co-occurrence evidence in blue, experimental evidence in purple, text mining evidence in yellow, database evidence in light blue, and co-expression evidence in black. As only yellow lines were observed on days 14 and 28, only text mining evidence was observed. The strength of alternative splicing (cellular enrichment) was 1.16 with an FDR (false discovery rate) of 0.0409.

The biological, and molecular enrichment processes were statistically insignificant. The predicted network includes only interactions with confidence scores that are higher than the lowest needed interaction score. Lower scores are associated with higher levels of engagement but lower false positive rates. The confidence score indicates the likelihood that a predicted association between two metabolic pathway proteins in the database actually exists. Limitations of confidence include: low confidence—at least 0.15; 0.4, medium confidence; 0.7; high confidence; the lowest level of confidence: 0.9

Microarrays are a powerful high-throughput technology that allows for a comprehensive examination of the genome's expression levels and the detection of gene expression changes without making any assumptions. Over the last decade, microarrays have been extensively employed in various studies to identify irregularities in gene expression associated with mental disorders. Apart from the hypothesis-driven approach that focuses on analyzing expression levels of specific candidate genes, transcriptomics research has the potential to uncover new biomarkers related to diverse mental illnesses. These biomarkers could prove valuable in developing innovative intervention strategies and implementing personalized medicine approaches.

PPIs are essential for predicting the function of target proteins and molecules' drug-like properties. Some of the biological processes that are controlled by PPIs include the regulation of metabolic and developmental processes as well as interactions between cells [15]. Finding information about protein communications helps with the determination of remedial targets [18]. Studies have shown that proteins with more connections (hubs) include families of enzymes, transcription factors, and intrinsically disordered proteins [19,20]. PPIs, on the other hand, have more involved processes and a broader regulatory scope. To better comprehend their significance in the cell, it is necessary to recognize various interactions and

determine their effects. One approach to analyzing PPIs is the *in-silico* approach. The fundamental interaction unit in STRING is the "functional association," or link between two proteins that together contribute to a particular biological function. In the analysis, there were no significant gene co-expression, co-occurrence, or fusions for the gene. Table 2 displays the string database analysis's findings.

In the study by Joshi *et al.* [7] by day 7, all rats administered EG developed hyperoxaluria, displayed a few crystal deposits on day 14 and had significant crystal deposition by day 28. Genes encoding NADPH Oxidases, macromolecular crystallization modulators, inflammasome activation genes, and osteogenic marker genes all showed significant changes in expression. The findings show significant differences between hyperoxaluria and renal alterations brought on by CaOx crystals. Inflammation and injury are mostly linked to crystal deposition, demonstrating the important function that crystal retention plays [7]. Microarray data analysis shows that the set of genes expressed differentially is different at 14 days (hyperoxaluric phase) compared to the same at 28 days (CaOx crystal deposition).

Ten miRNAs were the intersections of the projected miRNAs targeting these genes and the hub miRNAs identified by miRNA analysis. The interaction network identified two miRNAs, hsa-miR-6884-5p and hsa-miR-4653-5p, and the genes, CDHR4 and EGR2 as significant players at day 14 and day 28 respectively. These results helped to partially explain how dysregulated gene expressions influence the pathophysiology of hyperoxaluria is different from renal injury due to CaOx crystal deposition. Promising techniques include effective modifications of the miRNA-gene interactions in hyperoxaluria.

Since miRNAs can target over 60% of human genes, they are thought to play a significant and wide-ranging function in gene regulation [21,22]. According to prior research, miRNAs play important regulatory roles in the development, structure, and operation of the kidney, as well as in the regulation of fluid, electrolytes, acid-base balance, and blood pressure. They take part in pathogenic processes as well. In addition, serum and urine miRNA levels are generally stable regardless of storage conditions [23]. MiRNAs are unquestionably useful as kidney injury diagnostic and monitoring markers.

Oxalate-induced oxidative stress causes damage to cells, accompanied by renal deposition of CaOx crystals. Studies have highlighted the extensive functions of miRNAs (miRNAs)

Table 2. Enrichment of top 10 genes and their associated miRNAs on day 28.

Enrichment FDR	Fold Enrichment	Pathway	Genes	MiRNA
0.0156	817	Early growth response, N-terminal	EGR2	hsa-miR-6511a-5p,hsa-miR-3921,hsa-miR-3618,hsa-miR-1910-3p,hsa-miR-106b-5p,hsa-miR-20a-5p,hsa-miR-653-5p,hsa-miR-4653-5p,hsa-miR-4682,hsa-miR-506-3p
0.0156	817	Iodothyronine deiodinase	DIO3	hsa-miR-6787-3p,hsa-miR-4645-5p,hsa-miR-1185-2-3p,hsa-miR-1185-1-3p,hsa-miR-6720-5p,hsa-miR-4795-3p,hsa-miR-4755-3p,hsa-miR-6512-3p,hsa-miR-4417,hsa-miR-6833-3p
0.0156	817	Endoplasgmic reticulum vesicle transporter	ERGIC2	hsa-miR-627-3p,hsa-miR-32-5p,hsa-miR-4742-5p,hsa-miR-92a-3p,hsa-miR-92b-3p,hsa-miR-135b-5p,hsa-miR-135a-5p,hsa-miR-6719-3p,hsa-miR-194-5p,hsa-miR-548c-3p
0.0156	817	Fibrinogen alpha/beta chain family	FGG	hsa-miR-95-5p,hsa-miR-6759-5p,hsa-miR-5590-3p,hsa-miR-4795-3p,hsa-miR-551b-5p,hsa-miR-4714-5p,hsa-miR-6793-5p,hsa-miR-3123,hsa-miR-372-5p,hsa-miR-6748-5p
0.0156	817	Domain of unknown function (DUF3446)	EGR2	hsa-miR-6511a-5p,hsa-miR-3921,hsa-miR-3618,hsa-miR-1910-3p,hsa-miR-106b-5p,hsa-miR-20a-5p,hsa-miR-653-5p,hsa-miR-4653-5p,hsa-miR-4682,hsa-miR-506-3p
0.0156	817	Endoplasmic Reticulum-Golgi Intermediate Compartment (ERGIC)	ERGIC2	hsa-miR-627-3p,hsa-miR-32-5p,hsa-miR-4742-5p,hsa-miR-92a-3p,hsa-miR-92b-3p,hsa-miR-135b-5p,hsa-miR-135a-5p,hsa-miR-6719-3p,hsa-miR-194-5p,hsa-miR-548c-3p
0.0181	490.2	Early growth response, N-terminal, and NAB family	EGR2	hsa-miR-6511a-5p,hsa-miR-3921,hsa-miR-3618,hsa-miR-1910-3p,hsa-miR-106b-5p,hsa-miR-20a-5p,hsa-miR-653-5p,hsa-miR-4653-5p,hsa-miR-4682,hsa-miR-506-3p
0.0181	490.2	Fibrinogen alpha/beta chain family, and Alpha2-antiplasmin	FGG	hsa-miR-95-5p,hsa-miR-6759-5p,hsa-miR-5590-3p,hsa-miR-4795-3p,hsa-miR-551b-5p,hsa-miR-4714-5p,hsa-miR-6793-5p,hsa-miR-3123,hsa-miR-372-5p,hsa-miR-6748-5p
0.0181	490.2	Endoplasmic reticulum vesicle transporter , and MnmE helical domain	ERGIC2	hsa-miR-627-3p,hsa-miR-32-5p,hsa-miR-4742-5p,hsa-miR-92a-3p,hsa-miR-92b-3p,hsa-miR-135b-5p,hsa-miR-135a-5p,hsa-miR-6719-3p,hsa-miR-194-5p,hsa-miR-548c-3p
0.0279	245.1	Mixed, incl. fibrinogen alpha/beta chain family, and kringle	FGG	hsa-miR-95-5p,hsa-miR-6759-5p,hsa-miR-5590-3p,hsa-miR-4795-3p,hsa-miR-551b-5p,hsa-miR-4714-5p,hsa-miR-6793-5p,hsa-miR-3123,hsa-miR-372-5p,hsa-miR-6748-5p
0.0279	245.1	Opioid neuropeptide precursor, and Opioid receptor	OPRM1	hsa-miR-3163,hsa-miR-6833-3p,hsa-miR-138-5p,hsa-miR-1290,hsa-miR-5004-3p,hsa-miR-939-5p,hsa-miR-4282,hsa-miR-1303,hsa-miR-7159-3p,hsa-miR-5692a
0.0279	245.1	Glycosphingolipid biosynthesis—lacto and neolacto series	FUT2	hsa-miR-4729,hsa-miR-1273f,hsa-miR-664a-3p,hsa-miR-4755-3p,hsa-miR-4690-3p,hsa-miR-619-5p,hsa-miR-627-3p,hsa-miR-579-3p,hsa-miR-664b-3p,hsa-miR-5696
0.0285	222.8181818	Iodothyronine deiodinase, and Organic Anion Transporter Polypeptide (OATP) famil	DIO3	hsa-miR-6787-3p,hsa-miR-4645-5p,hsa-miR-1185-2-3p,hsa-miR-1185-1-3p,hsa-miR-6720-5p,hsa-miR-4795-3p,hsa-miR-4755-3p,hsa-miR-6512-3p,hsa-miR-4417,hsa-miR-6833-3p
0.0290	204.25	Mixed, incl. early growth response, n-terminal, and nab family	EGR2	hsa-miR-6511a-5p,hsa-miR-3921,hsa-miR-3618,hsa-miR-1910-3p,hsa-miR-106b-5p,hsa-miR-20a-5p,hsa-miR-653-5p,hsa-miR-4653-5p,hsa-miR-4682,hsa-miR-506-3p
0.0294	188.5384615	Mixed, incl. ferrous iron transport protein b, and rf-1 domain	ERGIC2	hsa-miR-627-3p,hsa-miR-32-5p,hsa-miR-4742-5p,hsa-miR-92a-3p,hsa-miR-92b-3p,hsa-miR-135b-5p,hsa-miR-135a-5p,hsa-miR-6719-3p,hsa-miR-194-5p,hsa-miR-548c-3p
0.0413	94.26923077	Mixed, incl. virion, and ptbp1, rna recognition motif 1	HNRNPA3	hsa-miR-1184,hsa-miR-4775,hsa-miR-582-5p,hsa-miR-758-3p,hsa-miR-4719,hsa-miR-30a-5p,hsa-miR-5003-3p,hsa-miR-30d-5p,hsa-miR-30e-5p,hsa-miR-548av-3p
0.0413	84.51724138	Mixed, incl. organic anion transporter polypeptide (oatp) family, and iodothyron	DIO3	hsa-miR-6787-3p,hsa-miR-4645-5p,hsa-miR-1185-2-3p,hsa-miR-1185-1-3p,hsa-miR-6720-5p,hsa-miR-4795-3p,hsa-miR-4755-3p,hsa-miR-6512-3p,hsa-miR-4417,hsa-miR-6833-3p

Enrichment FDR	Fold Enrichment	Pathway	Genes	MiRNA
0.0413	79.06451613	Virion, and RNA recognition motif	HNRNPA3	hsa-miR-1184,hsa-miR-4775,hsa-miR-582-5p,hsa-miR-758-3p,hsa-miR-4719,hsa-miR-30a-5p,hsa-miR-5003-3p,hsa-miR-30d-5p,hsa-miR-30e-5p,hsa-miR-548av-3p
0.0413	79.06451613	Glycoprotein	FUT2	hsa-miR-4729,hsa-miR-1273f,hsa-miR-664a-3p,hsa-miR-4755-3p,hsa-miR-4690-3p,hsa-miR-619-5p,hsa-miR-627-3p,hsa-miR-579-3p,hsa-miR-664b-3p,hsa-miR-5696
0.0413	76.59375	ZIP Zinc transporter, and Cation efflux family	SLC31A1	hsa-miR-6867-5p,hsa-miR-147a,hsa-miR-6780a-5p,hsa-miR-3689b-3p,hsa-miR-3689c,hsa-miR-1273h-5p,hsa-miR-30b-3p,hsa-miR-3689a-3p,hsa-miR-8063,hsa-miR-7853-5p

in various processes, including cellular responses to oxidative stress. According to Jiang *et al.'s* [24] study, miR-155-5p has been shown to promote kidney oxidative stress injury caused by oxalate and COM. Other studies have also indicated that certain miRNAs like miR-34a, miR-20b, and miR-30c can inhibit the adhesion or deposition of cell crystals both *in vitro* and *in vivo* [25,26]. Additionally, another study by Jiang *et al.* [24] revealed that the interaction between H19 and miR-216b contributes to renal tubular epithelial cell injury and oxidative stress injury induced by CaOx nephrocalcinosis through the HMGB1/TLR4/NF-κB pathway [27]. Similarly, miR-23 was found to decrease CaOx crystal deposition and kidney injury. Recent research demonstrated that nine miRNAs show different expression levels in the urine of CaOx patients compared to the normal population [28 ,29]. These findings collectively highlight the various roles played by miRNAs in the formation of CaOx stones.

CONCLUSION

The results have demonstrated the efficacy of bioinformatics exploration methods for screening prospective pathogenic genes and their causal mechanisms for kidney damage in the hyperoxaluric phase and crystal deposition phase. Microarray data analysis shows that the set of genes expressed differentially is different at 14 days (hyperoxaluric phase) compared to the same at 28 days (CaOx crystal deposition). The interaction network identified two miRNAs, hsa-miR-6884-5p and hsa-miR-4653-5p, and two genes CDHR4 and EGR2 as significant players. **I**t was possible to accurately predict potential biomarkers of kidney damage for hyperoxaluria as well as the oxalate crystal deposition phase of the kidney, which may provide some promising targets for the treatment of hyperoxaluria.

AUTHOR CONTRIBUTIONS

All authors made substantial contributions to the conception and design, acquisition of data, or analysis and interpretation of data; took part in drafting the article or revising it critically for important intellectual content; agreed to submit to the current journal; gave final approval of the version to be published; and agree to be accountable for all aspects of the work. All the authors are eligible to be an author as per the international committee of medical journal editors (ICMJE) requirements/guidelines.

FINANCIAL SUPPORT

There is no funding to report.

CONFLICTS OF INTEREST

The authors report no financial or any other conflicts of interest in this work.

ETHICAL APPROVALS

This study does not involve experiments on animals or human subjects.

DATA AVAILABILITY

All data generated and analyzed are included in this research article.

PUBLISHER'S NOTE

This journal remains neutral with regard to jurisdictional claims in published institutional affiliation.

REFERENCES

1. Asplin JR. Hyperoxaluric calcium nephrolithiasis. Endocrinol Metab Clin North Am. 2002;31:927–49.
2. Milliner DS. The primary hyperoxalurias: an algorithm for diagnosis. Am J Nephrol. 2005;25:154–60.
3. Robijn S, Hoppe B, Vervaet BA, D'Haese PC, Verhulst A. Hyperoxaluria: a gut-kidney axis? Kidney Int. 2011;80:1146–58.
4. Arena R, Cahalin LP. Evaluation of cardiorespiratory fitness and respiratory muscle function in the obese population. Prog Cardiovasc Dis. 2014;56:457–64.
5. Hoppe B, Langman CB. A United States survey on diagnosis, treatment, and outcome of primary hyperoxaluria. Pediatr Nephrol. 2003;18:986–91.
6. Spasovski G, Beck BB, Blau N, Hoppe B, Tasic V. Late diagnosis of primary hyperoxaluria after failed kidney transplantation. Int Urol Nephrol. 2010;42:825–29.
7. Joshi S, Wang W, Khan SR. Transcriptional study of hyperoxaluria and calcium oxalate nephrolithiasis in male rats: inflammatory changes are mainly associated with crystal deposition. PLoS One. 2017;12(11):e0185009.
8. Bhatt S, Gething PW, Brady OJ, Messina JP, Farlow AW, Moyes CL, *et al*. The global distribution and burden of dengue. Nature. 2013;496(7446):504–7.
9. Guzman MG, Harris E. Dengue. Lancet. 2015;385(9966):453–65.
10. Shahen M, Guo Z, Shar AH, Ebaid R, Tao Q, Zhang W, *et al*. Dengue virus causes changes of MicroRNA-genes regulatory network revealing potential targets for antiviral drugs. BMC Syst Biol. 2018;12(1):2.
11. Tsai CY, Lee IK, Lee CH, Yang KD, Liu JW. Comparisons of dengue illness classified based on the 1997 and 2009 World Health Organization dengue classification schemes. J Microbiol Immunol Infect. 2013;46(4):271–81.
12. Castro MC, Wilson ME, Bloom DE. Disease and economic burdens of dengue. Lancet Infect Dis. 2017;17(3):e70–e8.

13. Pei H, Zuo L, Ma J, Cui L, Yu F, Lin Y. Transcriptome profiling reveals differential expression of interferon family induced by dengue virus 2 in human endothelial cells on tissue culture plastic and polyacrylamide hydrogel. J Med Virol. 2016;88(7):1137–51.

14. Biswal S, Reynales H, Saez-Llorens X, Lopez P, Borja-Tabora C, Kosalaraksa P, *et al*. Efficacy of a tetravalent dengue vaccine in healthy children and adolescents. N Engl J Med. 2019;381(21):2009–19.

15. Moodie Z, Juraska M, Huang Y, Zhuang Y, Fong Y, Carpp LN, *et al*. Neutralizing antibody correlates analysis of tetravalent dengue vaccine efficacy trials in Asia and Latin America. J Infect Dis. 2018;217(5):742–53.

16. Chou CH, Shrestha S, Yang CD, Chang NW, Lin YL, Liao KW, *et al*. miRTarBase update 2018: a resource for experimentally validated microRNA-target interactions. Nucleic Acids Res. 2018;46(D1):D296–302.

17. Pu M, Chen J, Tao Z, Miao L, Qi X, Wang Y, *et al*. Regulatory network of miRNA on its target: coordination between transcriptional and post-transcriptional regulation of gene expression. Cell Mol Life Sci. 2019;76(3):441–51.

18. Ryan MM, Lockstone HE, Huffaker SJ, Wayland MT, Webster MJ, Bahn S. Gene expression analysis of bipolar disorder reveals downregulation of the ubiquitin cycle and alterations in synaptic genes. Mol Psychiatry. 2006;11:965–78.

19. Clifton NE, Hannon E, Harwood JC, Di Florio A, Thomas KL, Holmans PA, *et al*. Dynamic expression of genes associated with schizophrenia and bipolar disorder across development. Transl Psychiatry. 2019;9(1):74.

20. Kumar A, Pareek V, Singh HN, Faiq MA, Narayan RK, Raza K, Kumar P. Altered expression of a unique set of genes reveals complex etiology of schizophrenia. Front Psychiatry. 2019;10:906.

21. Panizo S, Martínez-Arias L, Alonso-Montes C, Cannata P, Martín-Carro B, Fernández-Martín JL, *et al*. Fibrosis in chronic kidney disease: pathogenesis and consequences. Int J Mol Sci. 2021;22(1):408. doi: https://doi.org/10.3390/ijms22010408

22. Carbonell T, Gomes AV. MicroRNAs in the regulation of cellular redox status and its implications in myocardial ischemia-reperfusion injury. Redox Biol. 2020;36:101607.

23. Peters LJF, Floege J, Biessen EAL, Jankowski J, van der Vorst EPC. MicroRNAs in chronic kidney disease: four candidates for clinical application. Int J Mol Sci. 2020; 21(18):6547. doi: https://doi.org/10.3390/ijms21186547

24. Jiang K, Hu J, Luo G, Song D, Zhang P, Zhu J, *et al*. miR-155-5p promotes oxalate- and calcium-induced kidney oxidative stress injury by suppressing MGP expression. Oxid Med Cell Longev. 2020 Mar 4;2020:5863617.

25. Wang B, He G, Xu G, Wen J, Yu X. miRNA-34a inhibits cell adhesion by targeting CD44 in human renal epithelial cells: implications for renal stone disease. Urolithiasis. 2019;48(2):109–16. doi: https://doi.org/10.1007/s00240-019-01155-9

26. Shi J, Duan J, Gong H, Pang Y, Wang L, Yan Y. Exosomes from miR-20b-3p-overexpressing stromal cells ameliorate calcium oxalate deposition in rat kidney. J Cell Mol Med. 2019;23(11):7268–78.

27. Liu H, Ye T, Yang X, Liu J, Jiang K, Lu H, *et al*. H19 promote calcium oxalate nephrocalcinosis-induced renal tubular epithelial cell injury via a ceRNA pathway. eBioMedicine. 2019;50:366–78. doi: https://doi.org/10.1016/j.ebiom.2019.10.059

28. Chen Z, Yuan P, Sun X, Tang K, Liu H, Han S, *et al*. Pioglitazone decreased renal calcium oxalate crystal formation by suppressing M1 macrophage polarization via the PPAR-gamma-miR-23 axis. Am J Physiol Renal Physiol. 2019;317(1):F137–51.

29. Liang X, Lai Y, Wu W, Chen D, Zhong F, Huang J, *et al*. LncRNA-miRNA-mRNA expression variation profile in the urine of calcium oxalate stone patients. BMC Med Genomics. 2019;12(1):57.